Jurnal Polimesin
Department of Mechanical Engineering
State Polytechnic of Lhokseumawe
http://e-jurnal.pnl.ac.id/polimesin

e-ISSN : 2549-1999 No. : 6 Month : December
p-ISSN : 1693-5462 Volume : 23 Year : 2025

Processing dates: received on 2025-11-11, reviewed on 2025-09-12, accepted on 2025-12-15 and online availability on 2025-12-31

# Numerical and experimental investigation of scaling laws in PLA octet-truss lattice structures under compression load

**Muhammad Yusri Dzal Yahya**[1], **Agus Sigit Pramono**[1*]
Department of Mechanical Engineering, Institut Teknologi Sepuluh Nopember, Surabaya 60111, Indonesia
*Corresponding author: pramono@me.its.ac.id

## Abstract

The demand for lightweight materials with superior strength-to-weight ratios in modern industry has driven innovation in architectural materials. Lattice structures, enabled by advances in Additive Manufacturing (AM), present a promising solution. However, their mechanical performance often deviates from theoretical predictions due to the complexity of the fabrication process, particularly in Fused Deposition Modeling (FDM) technology, which is prone to process defects and size effects. This study aims to address the discrepancy between scaling-law predictions and the actual mechanical response of an Octet-Truss lattice structure fabricated from Polylactic Acid (PLA) using FDM. This study specifically investigates the effects of geometric scaling up/down (0.75x, 1x, and, 1.25x) and the number of periodic unit cells (1 - 8) on compressive response up to the yield limit. To validate the compression behavior, this study combined Finite Element Analysis (FEA) with experimental compression testing of FDM-fabricated PLA specimens. A highly accurate linear regression model ($R^2$  99.7%) was formulated, relating maximum compression force (Fmax) to the number of unit cells (ncell), with FEA predictions aligning with experimental results within a 1.70% error margin. This empirical scaling law facilitates accurate predictions of load-bearing capacity across a range of lattice configurations (with cell sizes ranging from 15 to 25 mm cell sizes ) and load predictions ranging from 312 to 2,847 N for all tested configurations. This contributes to the development of a practical and reliable predictive design tool for lightweight structural engineering applications.

**Keywords:**
Scaling law, additive manufacturing, octet-truss, lattice structure, fused deposition modeling (FDM)

## 1 Introduction

Engineers require novel materials with superior properties compared to conventional bulk materials. High-tech fields such as aerospace, automotive, and healthcare consistently demand materials with unique combinations of properties. This is especially true for materials performance-to-weight ratio. This requirement is primarily driven by the need to conserve energy, enhance driving enjoyment, and increase payload capacity. In this context, lightweight materials are critically important [1].

Additive Manufacturing (AM), commonly referred to as 3D printing, has become a technical revolution in addressing this problem. AM's strategy approach of sequentially adding layers enables the fabrication of structures previously deemed impossible [2]. Fused Deposition Modeling (FDM) is a widely used AM technology because it is cost-effective, easy to use, and compatibility with various thermoplastic materials [3]. This technology also contributes to global sustainability efforts through the production of Polylactic Acid (PLA), a biopolymer made from renewable sources [4].

Contemporary advances in additive manufacturing (AM) have enabled the fabrication of previously infeasible geometries, particularly lattice structures with controlled topology and periodic cell arrangements. The topology, dimensions, and interconnectivity of these unit cells critically influence their macroscopic mechanical properties [5]. However, these specific attributes complicate mechanical analysis. Classical continuum mechanics cannot be applied to lattice structures in the same manner as it is applied to solid materials; for example, the relationship $\sigma = F/A$ does not adequately capture the behavior of these structures. The term "effective cross-sectional area" is ambiguous, as the projected area at a larger scale does not accurately represent the real size of the solid material that is holding the load. The load capacity of a structure is affected by both the total area of the material and its spatial arrangement [6].

In genuine engineering design, the most essential question is not "what is the effective stress?" but "what is the maximum load ($F_{max}$) that a part with this exact configuration can handle before it breaks down permanently?" [7]. We can't only answer this question; we also need to know how the number of unit cells ($n_{cell}$), which is a separate structural parameter, affects the weight a structure can hold. This paradigm substantiates the analytical framework of this study by establishing an innovative empirical link between $F_{max}$ and $n_{cell}$, serving as a reliable design instrument.

The Octet-Truss structure is one of the best stretching-dominated architectures of all the many types of lattice topologies [8]. It has a significant nodal connectivity ($Z = 12$) since its shape is made up of both tetrahedrons and octahedrons. This indicates that, according to Maxwell's stability criterion, axial strain often results in deformation rather than bending [9]. This property, which is mostly about stretching, should make the material work exceptionally well [10]. This feature, however, renders the Octet-Truss structure particularly sensitive to flaws with the FDM process, like voids, layers that don't adhere together properly, and sizes that aren't right [11]. These issues rapidly make the struts less strong along their axes, which is how they hold up the weight [12]. Because of this, the Octet-Truss structure makes the effects of FDM faults worse. This is a helpful model system for figuring out how much a printed product's performance differs from what it should be.

The traditional scaling law asserts a linear relationship between relative density and mechanical properties in mostly elongated materials. However, additional research has uncovered substantial discrepancies in components produced by additive manufacturing (AM) [13]. These inconsistencies mostly stem from manufacturing process challenges and the "size effect," which denotes the nonlinear variation in mechanical characteristics that happens when the dimensions of the structure are altered [14]. Most studies on scaling laws in lattice structures focus on metallic materials or theoretical simulations [10], [11], [13], [15], [16], also there is a lack of empirical studies assessing the scaling rule for FDM PLA Octet-Truss structures, especially when modifications are applied to the geometric scale and cell periodicity, particularly in the range $n_{cell}$ = 1 to 8. This study aims to fill this gap by (1) conducting a numerical analysis of the compression behaviour of PLA Octet-Truss lattice structures, (2) validating the numerical model through experimentation, and (3) formulating and quantifying a novel empirical scaling rule based on the number of unit cells.

## 2 Research methodology

This study outlines the numerical and experimental techniques utilized to examine the influence of scaling laws on the mechanical properties of Octet-Truss lattice structures constructed from Polylactic Acid (PLA) using Fused Deposition Modeling (FDM) technology. The systematic research process enables a comprehensive examination of these mechanical properties, integrating computer modeling and physical validation, as illustrated in Fig.1.

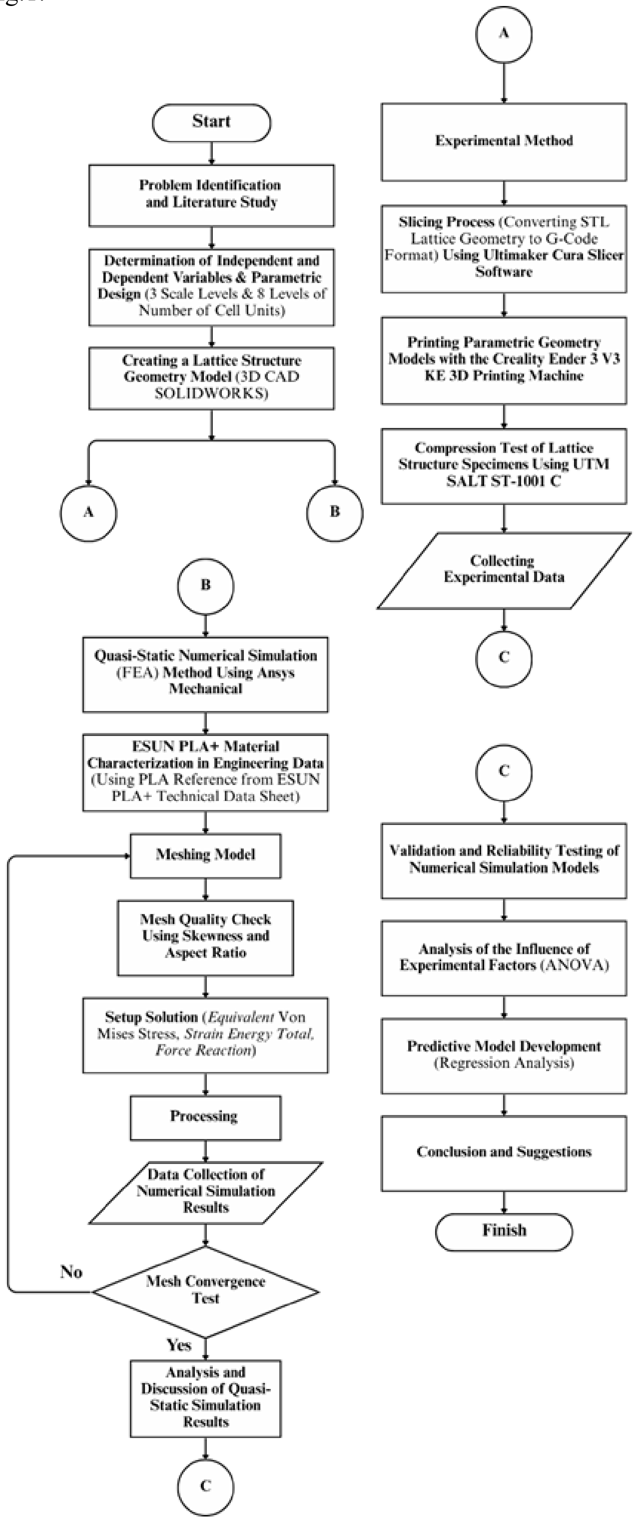

**Fig.1.** Research flowchart

## 2.1 Design and material specimens

### 2.1.1 Topology and material selection

The primary focus of this study is the examination of lattice structures characterized by Octet-Truss topology, as illustrated in Fig.2. This topology was selected due to its mechanical efficiency, particularly in terms of stiffness-to-weight and strength-to-weight ratios when compared to bending constructions [11].

The filament used is 1.75 mm wide and sourced from the ESUN PLA+ brand. It is made of polylactic acid, which stands for PLA. We chose PLA since it is one of the most common thermoplastic polymers used in Fused Deposition Modeling (FDM), owing to its affordability, ease of printing, availability, and biodegradability [17]. Additionally, PLA's well-documented mechanical properties facilitate straightforward modeling and study. Using filament from a single manufacturer and production batch for all specimens ensures material consistency.

### 2.1.2 Geometric design parameterization

We carefully changed two main independent variables to investigate how the lattice structure changed when the scale and cell number changed:

1. Geometric Scale: Three degrees of scale were employed to see how size affected things while retaining geometric congruence [18]. This means that the size of the unit cells relative to the strut remains the same, regardless of the scale. These scales are used:

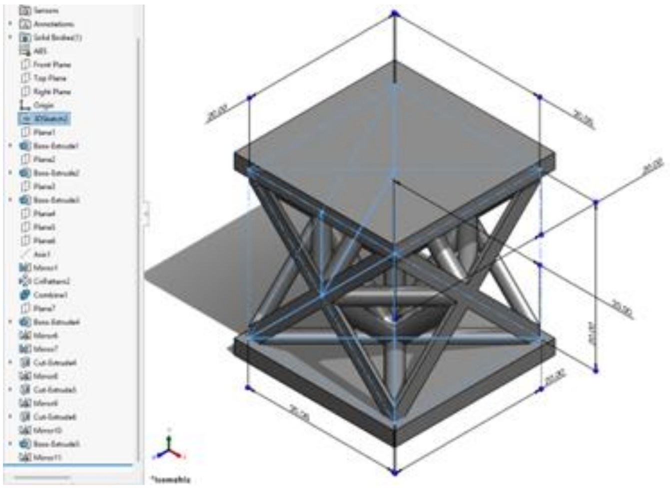

**Fig.2.** CAD octet-truss lattice modeling using SOLIDWORK 2025 software

- Scale Down (3:4): Cell dimensions 15x15x15 mm, strut diameter 1.5 mm.
- Normal Scale (1:1): Cell dimensions 20x20x20 mm, strut diameter 2 mm.
- Scale Up (5:4): Cell dimensions 25x25x25 mm, strut diameter 2.5 mm.

2. Number of Unit Cells: For each geometric scale, the number of unit cells ($n_{cell}$) is varied linearly along one axis (e.g., the X-axis or the width direction of the structure) from 1 to 8 cells ($n_{cell}$ = 1, 2, 3, 4, 5, 6, 7, 8) as shown in Fig.3 below. While the dimensions on the other two axes (Y and Z) are kept at one unit cell.

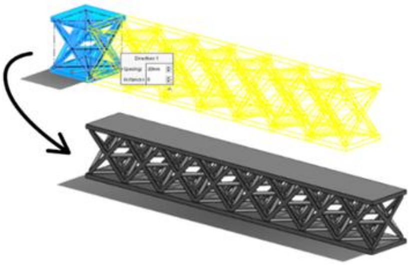

**Fig.3.** Process of increasing the number of lattice cell units using the linear pattern feature

The dependent variable, measured as the mechanical response of each configuration, is the Reaction Force in Newtons (N). This variable is assessed when the maximum von Mises stress reaches 63 MPa, corresponding to the yield strength ($\sigma_{yield}$) of the ESUN PLA+ in Table 2. This threshold was selected to focus the study on pre-yield mechanical behaviour, which is a critical design phase for engineering applications. The 63 MPa yield point marks the onset of plastic deformation, marking the material transitions from elastic to plastic response; thus, it serves as a practical reference for predicting load-bearing capacity in structural design. This threshold represents the yield strength of the ESUN PLA+ material used, allowing the study to focus specifically on pre-yield behaviour and plasticity initiation. of plasticity. A comprehensive Design of Experiments (DoE) matrix with 27 specimen configurations is presented in Table 1, ensuring systematic coverage of the investigated parameter space.

Table 1. Design of experiment (DoE) for all specimen configurations

| Specimen ID | Geometric Scale | Cell Dimensions (mm) |
|---|---|---|
| S1-C0..C8 | 3:4 | 15x15x15 |
| S2-C0..C8 | 1:1 | 20x20x20 |
| S3-C0..C8 | 5:4 | 25x25x25 |

### 2.2 Numerical analysis using finite element analysis (FEA)

We employed the Finite Element Method (FEA) in ANSYS Workbench software to run numerical simulations of lattice structures under compression loads. There are three elements to the simulation workflow: pre-processing, processing, and post-processing.

#### 2.2.1 Pre-processing

This stage involves preparing the model for analysis.

- Parametric Geometry Modeling: This step is all about getting the model ready to be seen. Using SOLIDWORKS 2025 CAD, we created all 24 Octet-Truss lattice geometry models, shown in Figure 4. It was straightforward to construct models with the same shape and size for any number of cells using 3D sketching, parametric, and linear pattern features.

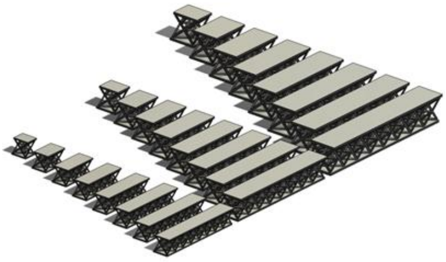

**Fig.4.** Experimental design number of cells and octet-truss lattice scaling size

- Meshing Procedure: The Meshing module in ANSYS Workbench is where the domain's shape is broken up into small pieces called finite elements. The lattice is hard to understand because it has cylindrical supports and connections between nodes. We used a tetrahedral element-based mesh, which can be seen in Fig.5, because it accurately represents curves and other geometric aspects [19].

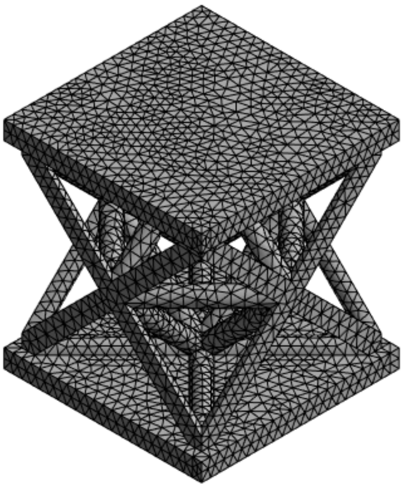

**Fig.5.** Lattice structure meshing process

a. Mesh Convergence Study: A mesh convergence study was conducted using the Octet-Truss 1x1x1 cell by varying the mesh density and evaluating key outputs such as maximum von Mises stress and response force, which is demonstrated in Fig.6. The optimal mesh was selected when changes in results were below 5%. All models were then analyzed using this mesh to ensure accurate FEA results.

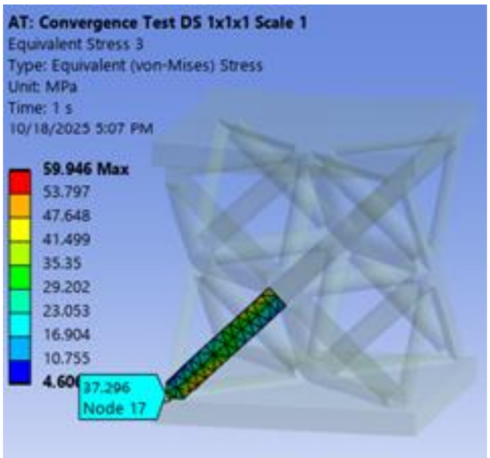

**Fig.6.** Determining the node that will be the reference for the comparison data for convergence

b. Mesh Quality Evaluation: We can use standard metrics like Skewness and Aspect Ratio in ANSYS to assess the quality of the mesh. We try to make sure that most of the parts, notably the most significant ones, meet the quality standards of skewness < 0.95 and aspect ratio < 10 [20]. This check is crucial to make sure that the prediction of local failure is correct.

- Material Definition: The ANSYS Engineering Data module creates a model of PLA material. We used the Technical Data Sheet (TDS) for ESUN PLA+, which we got from GB/T 1040 standard tensile testing [21], to pick the isotropic linear-elastic material model as the starting point. Table 2 lists the mechanical properties that were employed.

Table 2. PLA material properties used in simulations

| Material Properties | Value | Unit |
|---|---|---|
| Young's Modulus (E) | 1.973 | Gpa |
| Poisson's Ratio ($\nu$) | 0.35 | - |
| Yield Strength ($\sigma_{yield}$) | 63 | MPa |
| Ultimate Tensile Strength ($\sigma_{UTS}$) | 74 | MPa |

Given the elastoplastic complexity, the adoption of an isotropic linear-elastic model is justified by three key factors: (1) Yield Point Focus: The analysis is strictly bounded at the 63 MPa yield threshold. Below this point, PLA exhibits predominantly linear behavior, making the elastic model effective for predicting safe load-bearing capacity. (2) Scope Limitation: The study specifically targets the elastic-plastic transition, intentionally excluding post-yield mechanics, such as strain hardening or collapse, from its scope. (3) Computational Efficiency: For the 24-configuration parameter space, the linear-elastic model ensures solution stability and rapid convergence in ANSYS, offering an optimal balance between efficiency and pre-yield accuracy without the significant overhead associated with non-linear calibration.

- Boundary Conditions: To accurately replicate the experimental compression test, the following boundary conditions will be implemented as shown in Figure 7: a fixed support on the bottom surface of the lattice structure to constrain all translational and rotational degrees of freedom, and a load on the top surface to evaluate the structure's vertical safety and resilience response (negative Y-axis). The analytical boundary conditions dictate that the static compression simulation is configured to ensure that the load results in a maximum equivalent stress value of 63 MPa.

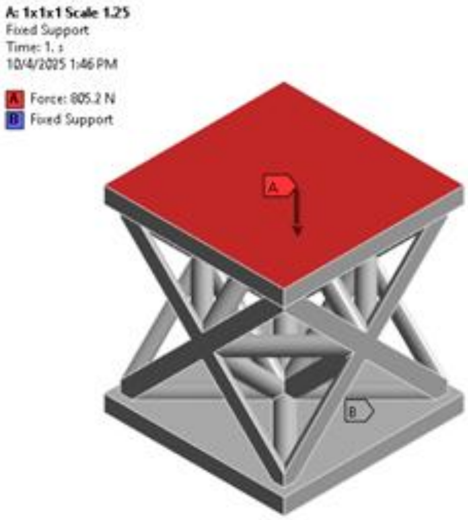

**Fig.7.** Boundary condition: (a) loading, (b) support

### 2.2.2 Processing

The discretized model goes through a computation process called "running" during the processing stage. Peter Newman (2018) [22], a structural analyst at Ansys, says that the user must first enter Young's Modulus (E), Poisson's ratio (v), boundary conditions (supports), and loads before the solution process can begin. Then, the computer uses Hooke's Law, F = [K].x, to solve the matrix equation and obtain the vectors of nodal displacements (x). Once we know how far each node has traveled, we can find the strain values. After that, the strains are used to determine the stress at each node. After that, the stresses are adjusted to obtain the main stress values, and a map is made to show where they are so the model can determine its most important stressors.

### 2.2.3 Post-processing

During the post-processing stage, the data from the computer simulation is examined. Now, the data is shown at each node to show how the response is spread out across the full object, as illustrated in Figure 8. The results demonstrate how the equivalent stress (von Mises), equivalent strain, displacement, and reaction forces at the supports are spread out. The research is founded on the identified critical stress levels within these distributions.

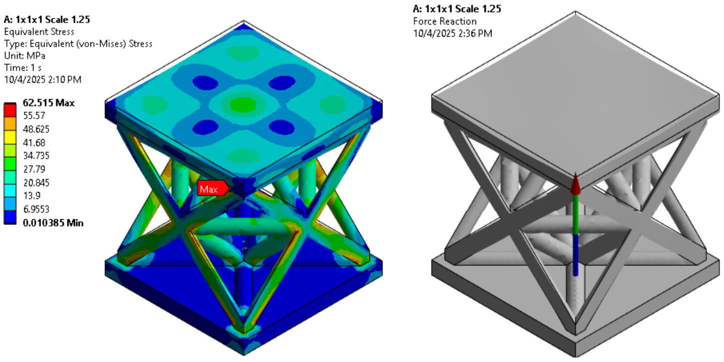

**Fig.8.** Desired simulation response results

The von Mises equivalent stress is the lowest value used for metals and many polymers in assessing multi-axial tensile/compressive failure. The stress components characterize Von-Mises ($\sigma_v$) as follows [23]:

$$\sigma_v = \sqrt{\frac{1}{2}\left[(\sigma_{11}-\sigma_{22})^2+(\sigma_{22}-\sigma_{33})^2+(\sigma_{33}-\sigma_{11})^2\right]+3\left({\tau_{12}}^2+{\tau_{23}}^2+{\tau_{31}}^2\right)} \quad (1)$$

To make a force-displacement curve that looks like the data from the experiment. To get the nominal stress in the sample, divide the force reaction F by the area that is projected appropriately [7].

$$\sigma_{nominal} = \frac{F}{A} \quad (2)$$

Strain energy is a basic measure of a structure's ability to store energy. In the linear-elastic case, the elastic strain energy density (strain energy density) for a particular column is shown as [24]:

$$u = \frac{1}{2}\sigma_{ij}\varepsilon_{ij} \quad (3)$$

The total strain energy up to a specific load point is the integral of the stress over the strain or the integral of the force over the displacement, as shown below [25].

$$U = \int_0^{\varepsilon} \sigma(\varepsilon)\, d\varepsilon \text{ or } U = \int_0^{\delta} F(\delta)\, d\delta \quad (4)$$

### 2.3 Specimen fabrication using fused deposition modeling (FDM)

The Octet-Truss lattice samples were made using FDM technology. To make the print more accurate, a lot of work went into making sure the process was the same every time and under control. This made it possible to reliably link any changes in the mechanical reaction to the design factors, namely, the number of cells and the geometric scale.

### 2.3.1 Equipment and material specifications

All samples were created on a single Creality Ender-3 V3 KE 3D printer, as shown in Fig.9. We chose this machine because it was available and could produce prints good enough for this study. If we just utilize one machine, there can't be any discrepancies between them. The ESUN PLA+ filament used to make all samples has a diameter of 1.75 mm.

**Fig.9.** Creality ender-3 V3 KE 3D printer unit

### 2.3.2 Equipment and Material Specifications

To ensure that all 24 specimen design configurations were printed the same way and to minimize the effects of manufacturing variability, the same printing parameters were used for all of them. We set these settings using Ultimaker Cura 5.10.2 slicer software (Fig.10) and profiles for the Ender-3 V3 KE printer (Figure 11). Table 3 provides a quick overview of the key points.

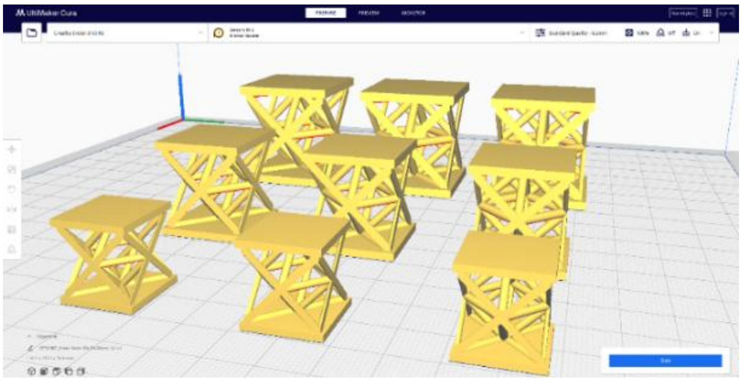

**Fig.10.** Process of exporting geometry models from solidworks 2025 CAD software to STL format using ultimaker cura 5.10.2 software

Table 3. Standard FDM printing parameters for PLA specimen fabrication

| Slicer Parameters | Specified Values | Justification |
|---|---|---|
| Nozzle Temperature | 210 °C | Optimal temperature for layer adhesion and flow of standard PLA filament. |
| Print Bed Temperature | 60 °C | Prevents warping and ensures good adhesion of the first layer. |
| Layer Height | 0.2 mm | Good balance between print speed and vertical resolution. |
| Print Speed | 300 mm/s | Conservative speed to ensure geometric accuracy on complex lattice structures. |
| Infill Density | 100% | Ensures fully dense printed specimens match the CAD model. |
| Infill Pattern | Lines / Rectilinear | Simple and efficient patterning for 100% infill. |
| Number of Walls | 3 | Provides adequate perimeter strength. |
| Retraction | Enabled | Prevents stringing or oozing between separate parts of the model. |
| Retraction Distance | 0.8 mm | Typical values for direct-drive extruders. |
| Retraction Speed | 40 mm/s | Typical values for direct-drive extruders. |
| Cooling (Fan) | 100% | Critical for rapid PLA cooling to maintain lattice geometry |

The 100% infill setting aims to create struts that are as dense as possible, approximating the ideal CAD model. However, it is crucial to recognize that the FDM process is inherently prone to producing microstructural defects such as small voids between filament paths (rasters) or between layers, even at the 100% infill setting.

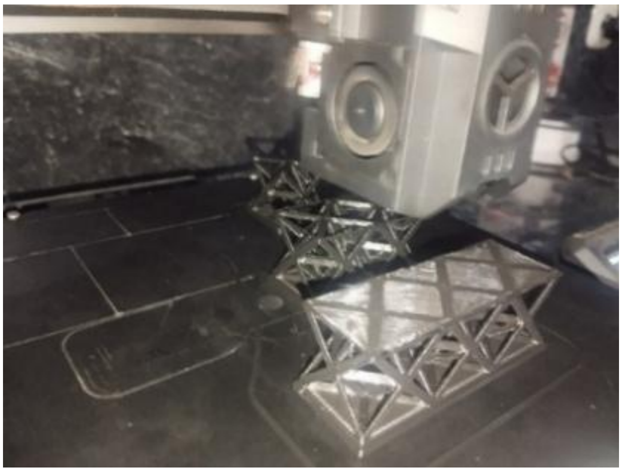

**Fig.11.** Lattice geometry model fabrication process using 3D printing ender-3 V3 KE

To control FDM-induced anisotropy, all specimens were printed with a consistent vertical Z-axis orientation (Figure 12). This ensured uniform diagonal strut angles relative to the deposition layers across all samples [26]. providing a consistent baseline for comparison despite unavoidable stair-stepping artifacts on sloped surfaces.

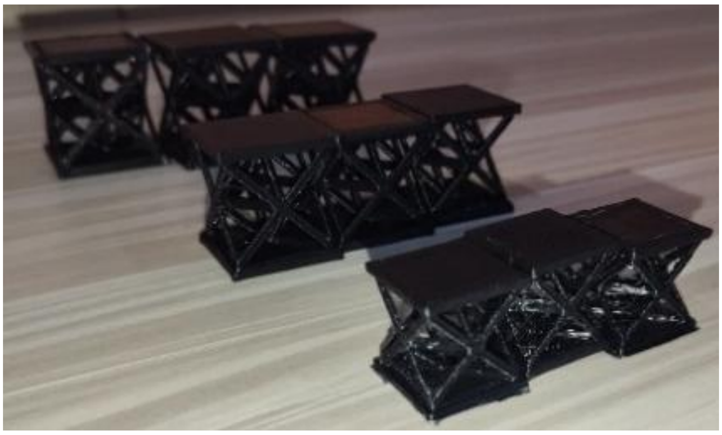

**Fig.12.** Results of the 3D printing fabrication process for the octet-truss lattice model

## 2.4 Experimental compression testing

### 2.4.1 Compression test standards and procedures

Uniaxial compression testing followed ASTM D695 principles [27], adapted for lattice structures up to the yield point (Table 4). Experiments were conducted using a SALT ST-1001 C Universal Testing Machine (Fig.13) equipped with a 10 kN load cell and rigid parallel steel plates.

Table 4. Compression test parameters according to ASTM D695 principles

| Testing Parameters | Values/Specifications |
|---|---|
| Reference Standard | ASTM D695-15 |
| Specimen Geometry | Lattice Structure (Cuboidal) |
| Conditioning Temperature | 23 ± 2 °C |
| Conditioning Relative Humidity | 50 ± 5% |
| Minimum Conditioning Duration | 40 hours |
| Test Speed (Crosshead) | 5 mm/min |
| Number of Replications per Design | Minimum 3 |

### 2.4.2 Equipment configuration and data acquisition

Testing was conducted using a SALT ST-1001 C Universal Testing Machine (UTM) shown in Fig.13, equipped with a 10 kN load cell for accurate compression force measurement. The machine is equipped with a pair of flat, parallel, rigid steel compression plates.

**Fig.13.** Quasi-static compression test setup using the SALT ST-1001 C UTM machine

Specimens were carefully centered to ensure concentric loading and prevent premature buckling or artificial failure modes caused by misalignment (Fig.14). Force and displacement data were acquired simultaneously via a digital interface with a 10 Hz sampling rate to accurately capture the force-displacement response.

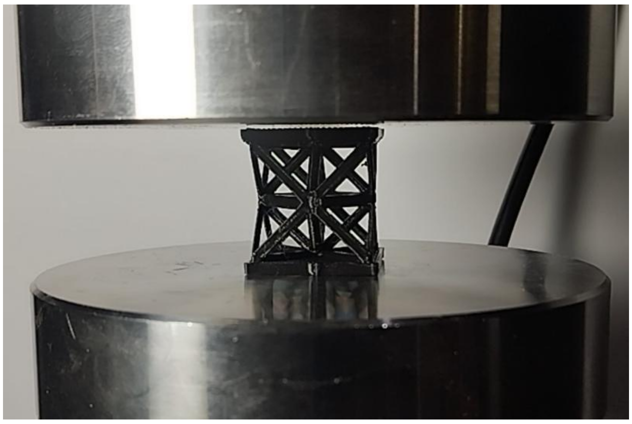

**Fig.14.** Placement of fixtures and specimens on the UTM machine for ASTM D695 compression testing

### 2.4.3 Testing and Failure Observation

Following measurement and preloading, compression was applied at 5 mm/min until significant load drop or densification. Force-displacement curves were recorded to extract yield and maximum forces (Fig.15), with a minimum of three replicates per configuration. Failure modes, including buckling, fracture, and delamination, were documented through imaging.

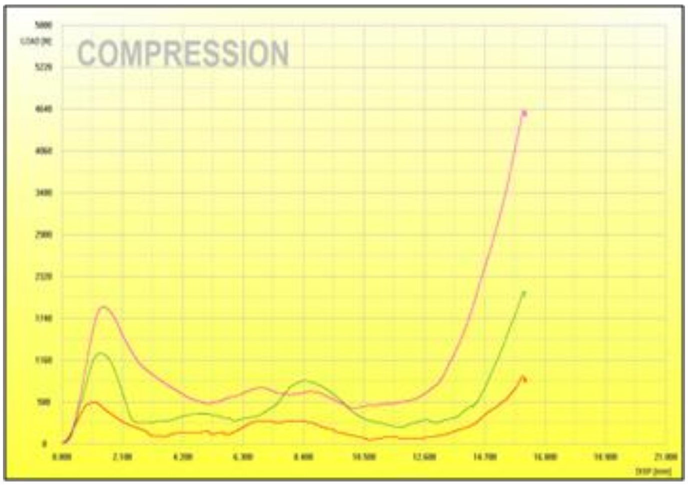

**Fig.15.** Load-displacement graph results of compression testing read by monitor

### 2.5 Data analysis methods

To achieve the research goals, statistical and quantitative methodologies were used to analyze data from numerical simulations and experimental tests.

#### 2.5.1 Experimental data processing

The raw force-displacement curves from each compression test (using three replicates) were processed to extract key parameters. The maximum force at the yield point ($F_{\max,\text{exp}}$) was identified as the peak force value on the curve before significant load reduction or densification occurred.

#### 2.5.2 FEA model validation

FEA model validation is performed by comparing its predictions to experimental data.

- Quantitative Comparison: The reaction force values at yield extracted from the FEA simulation ($F_{\text{sim}}$) are compared directly with the average maximum force values from the experiment $(\bar{F}_{\max,\text{exp}})$.
- Error Margin Analysis: To quantify the level of fit, an error margin metric is calculated for each configuration. The Mean Absolute Percentage Error (MAPE) can be used as an overall measure of model accuracy across the design space [28].

$$MAPE = \frac{100\%}{n}\sum_{i=1}^{n}\left|\frac{F_{sim,i}-\bar{F}_{\max,\text{exp}}}{\bar{F}_{\max,\text{exp}}}\right| \qquad (6)$$

where N = 3 is the number of design configurations.

- Qualitative Comparison: The deformation patterns predicted by FEA at the yield state are visually compared with the failure modes observed in the experimental specimens.

#### 2.5.3 Empirical scaling law analysis

The reaction force data on yield from validated FEA simulations ($F_{\text{sim}}$) are used as the basis for deriving empirical scaling laws.

- Verification of Regression Assumptions: Before applying linear regression, the assumption of normality of the $F_{\text{sim}}$ data for each geometric scale group (0.75x, 1x, 1.25x) was verified using statistical tests such as the Anderson-Darling test. The results of the normality test (P-value > 0.05) supported the use of a linear regression model.
- Linear Regression Analysis: For each of the three geometric scale groups, a simple linear regression analysis was performed with $F_{\text{sim}}$ as the dependent variable (Y) and the Number of Unit Cells ($n_{\text{cell}}$) as the independent variable (X). The regression model took the form:

$$F_{\max} = m \times n_{\text{cell}} + C \qquad (7)$$

estimated using the Ordinary Least Squares (OLS) method.

- Regression Model Evaluation: The quality and significance of each regression model is evaluated based on:
  a. Coefficient of Determination ($R^2$ and $R^2_{\text{adj}}$): Measures the proportion of $F_{\text{sim}}$ variance that can be explained by $n_{\text{cell}}$. An $R^2$ value close to 1 indicates excellent goodness-of-fit. The $R^2$ formula is given by the following.

$$R^2 = \frac{SS_{res}}{SS_{tot}} = 1 - \frac{\Sigma(y_i-\hat{y}_i)^2}{\Sigma(y_i-\bar{y})^2} \qquad (8)$$

  b. Statistical Significance: The P-value from the F test (regression ANOVA) is used to assess the overall significance of the model [29]. The p-values for the slope coefficient (m) and the intercept (c) were used to assess the significance of each parameter. The significance level (α) was set at 0.05.

$$F = \frac{MSB}{MSW} = \frac{SSB\ /\ (k-1)}{SSW\ /\ (N-k)} \qquad (9)$$

  Where SSB is the Sum of Squares Between (between groups), SSW is the Sum of Squares Within (within groups), k is the number of groups, and N is the total number of observations. A large F-value indicates that the influence of the factor is more significant than random variation. If the ANOVA shows a significant effect, a post-hoc test (e.g., Tukey's HSD) is used for pairwise comparisons.

  c. Residual Analysis: Residual plots (e.g., Residuals vs. Fits, Normal Probability Plot) are examined to validate the assumptions of linear regression (linearity, normality of errors, homoscedasticity, independence of errors).

- Interpretation of Scaling Law Parameters: The slope coefficient (m) of each regression model is interpreted as an empirical scale factor that quantifies the average additional force contribution from each additional unit of lattice cell at that geometric scale. A comparison of m values between geometric scales ($m_{0.75x}$, $m_{1x}$, $m_{1.25x}$) is used to analyze the size effect on the $F_{\text{sim}}$ vs $n_{\text{cell}}$ relationship.

## 3 Result and discussion

### 3.1 Characterization of numerical simulation (FEA) results

FEA simulations provide predictions of the mechanical behaviour of lattice structures under ideal conditions (perfect geometry, isotropic homogeneous material).

#### 3.1.1 Mesh convergence and quality

Using a standard model (1x1x1 cell), mesh-convergence research showed that the simulation results (maximum von Mises stress and reaction force) converged at a given mesh-density threshold. Fig. 16's convergence charts show that increasing the mesh accuracy didn't change the result by more than 5%. After that, all 24 models employed the converged mesh density.

Table 5. Mesh convergence test octet truss lattice

| Element | Stress (MPa) | Error (%) |
|---|---|---|
| 4138 | 25.80 | |
| 4289 | 28.09 | 8.17 |
| 4479 | 30.17 | 6.88 |
| 4963 | 29.71 | 1.54 |
| 7658 | 33.57 | 11.50 |
| 9498 | 34.07 | 1.46 |
| 14243 | 36.22 | 5.93 |
| 26487 | 37.63 | 3.76 |
| 35907 | 38.00 | 0.97 |
| 50833 | 38.08 | 0.21 |

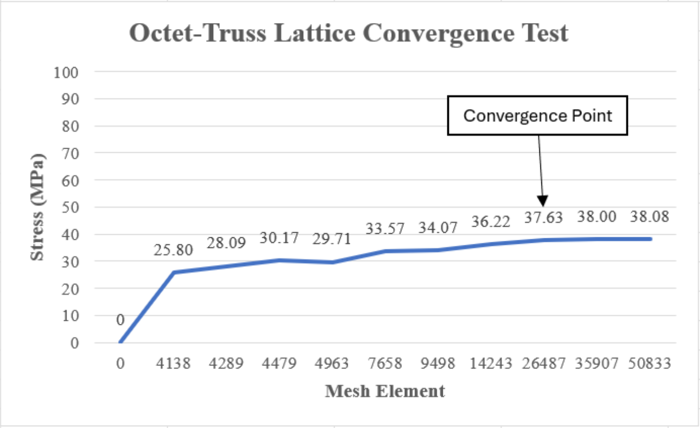

**Fig.16.** Load-mesh element curve for convergence test

Mesh quality evaluation using Skewness and Aspect Ratio metrics in ANSYS shows that most elements are in the good-to-excellent quality range, with the worst mesh quality values at skewness 0.867 and maximum aspect ratio 6.94, as shown in Figure 17 below.

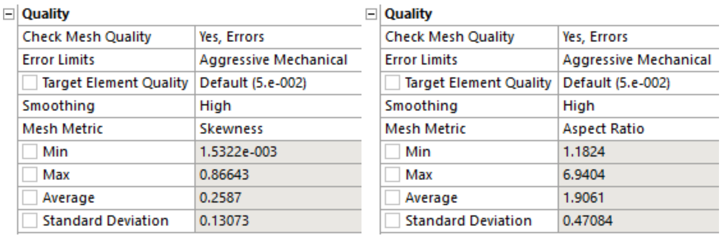

| Quality | |
|---|---|
| Check Mesh Quality | Yes, Errors |
| Error Limits | Aggressive Mechanical |
| ☐ Target Element Quality | Default (5.e-002) |
| Smoothing | High |
| Mesh Metric | Skewness |
| ☐ Min | 1.5322e-003 |
| ☐ Max | 0.86643 |
| ☐ Average | 0.2587 |
| ☐ Standard Deviation | 0.13073 |

| Quality | |
|---|---|
| Check Mesh Quality | Yes, Errors |
| Error Limits | Aggressive Mechanical |
| ☐ Target Element Quality | Default (5.e-002) |
| Smoothing | High |
| Mesh Metric | Aspect Ratio |
| ☐ Min | 1.1824 |
| ☐ Max | 6.9404 |
| ☐ Average | 1.9061 |
| ☐ Standard Deviation | 0.47084 |

**Fig.17.** Mesh quality check using skewness and aspect ratio

### 3.1.2 Stress distribution

Visualization of the FEA results at the yield limit state ($\sigma_{v,max} \approx$ 63 MPa) provides insight into the structural response mechanism. The von Mises equivalent stress contours consistently show the highest stress concentrations at node connections and/or in the middle of the struts, where secondary bending stresses arise from global deformation. The specific locations of the highest stress concentrations may vary slightly depending on the scale and number of cells, but the patterns are generally similar, indicating that yielding is likely to initiate in these regions.

### 3.1.3 Reaction force at yield ($F_{sim}$)

The total reaction force values at the top plate ($F_{sim}$) extracted from each simulation at $\sigma_{v,max} \approx$ 63 MPa are tabulated in Figure 18 and Table 6 for all 27 design configurations. This data is the primary quantitative output of the FEA simulation and serves as the basis for validation and scaling law analysis.

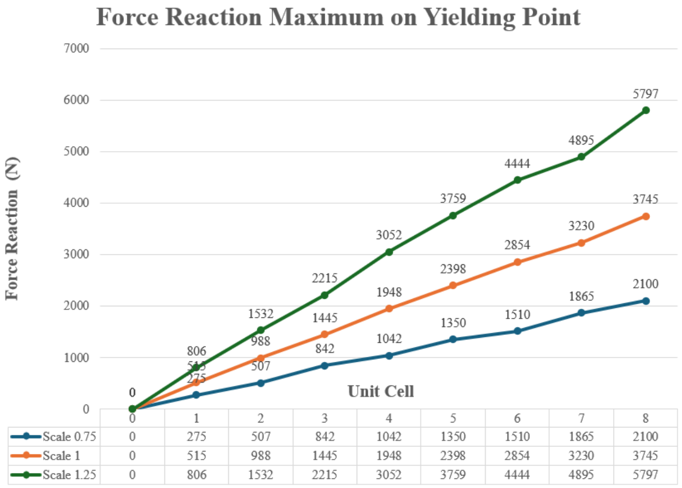

| | 0 | 1 | 2 | 3 | 4 | 5 | 6 | 7 | 8 |
|---|---|---|---|---|---|---|---|---|---|
| Scale 0.75 | 0 | 275 | 507 | 842 | 1042 | 1350 | 1510 | 1865 | 2100 |
| Scale 1 | 0 | 515 | 988 | 1445 | 1948 | 2398 | 2854 | 3230 | 3745 |
| Scale 1.25 | 0 | 806 | 1532 | 2215 | 3052 | 3759 | 4444 | 4895 | 5797 |

**Fig.18.** Comparison of reaction force results at the yield limit with 3 different scales

Table 6. Summary of total strain energy (mJ) and reaction force ($F_{sim}$) results of FEA simulation at yield limit ($\sigma_{v,max}$ = 63 MPa)

| Specimen ID | Geometric Scale | Number of Unit Cells | Strain Energy Total (mJ) | $F_{sim}$ (N) |
|---|---|---|---|---|
| S1-C0 | 3:4 | 0 | 0 | 0 |
| S1-C1 | 3:4 | 1 | 76.04 | 275 |
| S1-C2 | 3:4 | 2 | 122.98 | 507 |
| S1-C3 | 3:4 | 3 | 222.12 | 842 |
| S1-C4 | 3:4 | 4 | 252.81 | 1042 |
| S1-C5 | 3:4 | 5 | 337.46 | 1350 |
| S1-C6 | 3:4 | 6 | 350.36 | 1510 |
| S1-C7 | 3:4 | 7 | 456.55 | 1865 |
| S1-C8 | 3:4 | 8 | 505.21 | 2100 |
| S2-C0 | 1:1 | 0 | 0 | 0 |
| S2-C1 | 1:1 | 1 | 199.91 | 515 |
| S2-C2 | 1:1 | 2 | 350.30 | 988 |
| S2-C3 | 1:1 | 3 | 490.60 | 1445 |
| S2-C4 | 1:1 | 4 | 662.68 | 1948 |
| S2-C5 | 1:1 | 5 | 798.53 | 2398 |
| S2-C6 | 1:1 | 6 | 938.65 | 2854 |
| S2-C7 | 1:1 | 7 | 1027.1 | 3230 |
| S2-C8 | 1:1 | 8 | 1205.1 | 3745 |
| S3-C0 | 5:4 | 0 | 0 | 0 |
| S3-C1 | 5:4 | 1 | 391.83 | 806 |
| S3-C2 | 5:4 | 2 | 673.78 | 1532 |
| S3-C3 | 5:4 | 3 | 922.37 | 2215 |
| S3-C4 | 5:4 | 4 | 1301.20 | 3052 |
| S3-C5 | 5:4 | 5 | 1570 | 3759 |
| S3-C6 | 5:4 | 6 | 1820.9 | 4444 |
| S3-C7 | 5:4 | 7 | 1887.5 | 4895 |
| S3-C8 | 5:4 | 8 | 2310.1 | 5797 |

## 3.2 Characterization of experimental results

Compression testing of physical specimens shown in Fig.19 provides ground-truth data on the actual mechanical behaviour of FDM-derived PLA lattice structures.

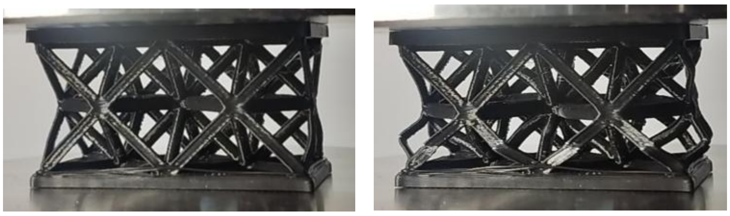

**Fig.19.** Observation of specimen deformation behaviour in compression testing

### 3.2.1 Experimental force-displacement curves

A typical force-displacement curve from UTM testing, shown in Fig.15 above, consists of an initial linear region (elastic response), a peak load indicating yield or failure initiation, and post-peak softening due to buckling or fracture. At large displacements, a plateau or densification region may appear, reflecting stable failure or structure densification. This failure mode is consistent with theoretical predictions for stretching-dominated lattices under axial compression: in the Octet-Truss, load primarily transfers through axial strut forces rather than bending, making the structure sensitive to imperfection-triggered buckling [11]. These features also align with the observed behaviour of cellular or lattice materials under compression.

### 3.2.2 Reaction force at yield ($F_{max,exp}$)

The maximum force values ($F_{max,exp}$) identified from each compression test curve were processed. Table 7 below presents a summary of the maximum force results from the experimental tests at the yielding limit, with three repetitions of 1.25-scale lattice samples, totaling 1 unit cell.

Table 7. Summary of the maximum force results from the experimental compression test at the yielding limit.

| Specimen ID | Geometric Scale | Number of Unit Cells | $F_{max,exp}$ (N) |
|---|---|---|---|
| S3-C1 (1) | 5:4 | 1 | 807 |
| S3-C1 (2) | 5:4 | 1 | 779 |
| S3-C1 (3) | 5:4 | 1 | 794 |

### 3.3 FEA model validation

Quantitative validation was achieved by comparing the FEA-predicted yield force values ($F_{sim}$) with the empirically derived average values ($F_{max,exp}$).

### 3.3.1 Quantitative force comparison

We compared the maximum reaction force values from the FEA simulation ($F_{sim}$ in Table 6) with the experimental compression test ($F_{max,exp}$ in Table 7) on the validation specimen (1x1x1 configuration, scale 1.25, n = 3). Table 8 shows that the mean margin of error (MAPE) was 1.70% when the force values were compared directly. The FEA model is a highly accurate "digital twin" of the real specimen, with a low error rate and statistical validation.

Table 8. Comparison of reaction forces and error margin calculations for model validation

| Specimen ID | $F_{sim}$ | $F_{max,exp}$ | Error Margin (%) |
|---|---|---|---|
| S3-C1 (1) | 806 | 807 | 0.12 |
| S3-C1 (2) | 806 | 779 | 3.47 |
| S3-C1 (3) | 806 | 794 | 1.51 |
| Average MAPE | | | 1.70 |

### 3.4 Scaling law analysis and the influence of design parameters

This study investigates the relationship between the yield reaction force ($F_{sim}$, obtained from validated FEA data) and the number of unit cells ($n_{cell}$) for each geometric scale, to develop an empirical scaling law.

### 3.4.1 Normality testing of simulated reaction force data

Before conducting the regression analysis, a normality test was performed on the simulated reaction force data to ensure that it met the basic assumptions of linear regression. The Anderson-Darling normality test was applied to data from all three scale variations. The results, as shown in Table 9, indicate that all data sets (from 0 to 8 unit cells lattices) are normally distributed. The p-value for each scale (scaled down, normal scale, and scaled up) is significantly greater than the general significance level ($\alpha = 0.05$), thus failing to reject the null hypothesis (that the data are normally distributed).

Table 9. Results of the anderson-darling normality test for all variations of the octet-truss lattice unit cells scale

| Geometric Scale | Average (Mean) | Standard Deviati (StDev) | P-Value |
|---|---|---|---|
| *Scale-down* (3:4) | 1055 | 716.7 | 0.959 |
| *Normal* (1:1) | 1903 | 1270 | 0.963 |
| *Scale-up* (5:4) | 2944 | 1957 | 0.953 |

### 3.4.2 Analysis of the effect of scaling and number of cells

Using the validated FEA model, a comprehensive analysis was performed to investigate the effects of geometric scale and the number of unit cells on the compressive load capacity. The results of 24 simulations show a clear, consistent trend: Fig.20 for Scale Down, Fig.23 for Normal Scale, and Fig.26 for Scale Up. When the maximum force ($F_{max}$) is plotted against the number of unit cells ($n_{cell}$) for each of the three geometric scales (scale-down, normal, scale-up), a strong linear relationship is observed. For each scale, systematically increasing the number of unit cells results in a proportional increase in the maximum load capacity. This data visualization strongly indicates that the mechanical behaviour of the structure can be modeled by a simple linear equation of the form $F_{max} = m.n_{cell} + c$, where the coefficients m and c depend on the geometric scale of the structure.

### 3.4.3 Empirical scaling law formulation

To quantify the observed linear relationship, a linear regression analysis was performed on the validated simulation data. A parametric study involving 24 FEA simulations yielded data on the relationship between the number of unit cells and the load-bearing capacity (maximum reaction force) for each of the three geometric scales. The ANOVA results are shown in Fig.21 (Scale Down), 24 (Normal Scale), and 27 (Scale Up), and the residual analysis is shown in Fig.22 (Scale Down), 25 (Normal Scale), and 28 (Scale Up). These data were then used to assess significance and validate the model assumptions for linear regression analysis, and the results are presented in Table 10.

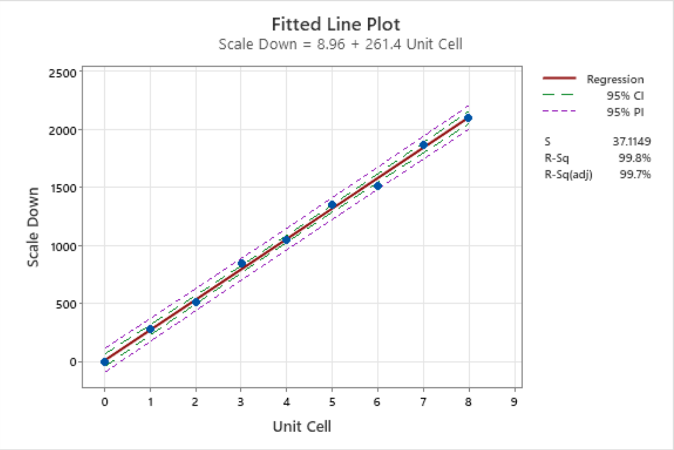

**Fig.20.** Scale down unit cells lattice regression equation

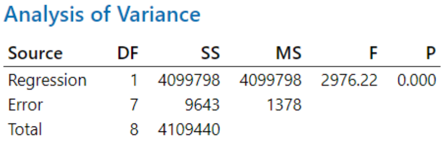

Analysis of Variance

| Source | DF | SS | MS | F | P |
|---|---|---|---|---|---|
| Regression | 1 | 4099798 | 4099798 | 2976.22 | 0.000 |
| Error | 7 | 9643 | 1378 | | |
| Total | 8 | 4109440 | | | |

**Fig.21.** ANOVA results of the relationship between unit cells Lattice scale down and maximum force reaction during yielding

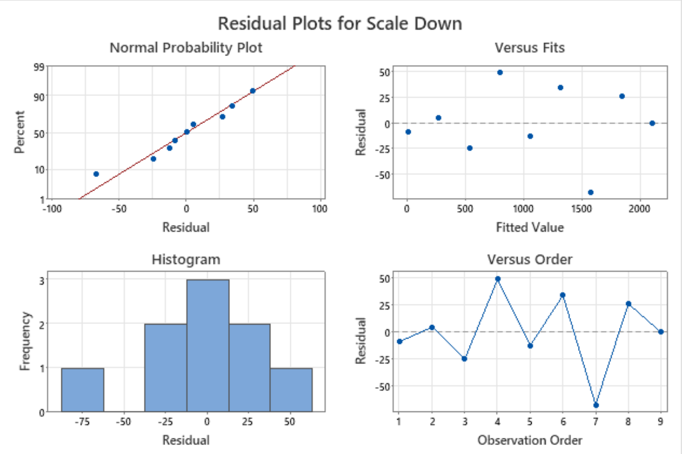

**Fig.22.** Validation of model assumptions (residual analysis) of the scaled down linear regression model

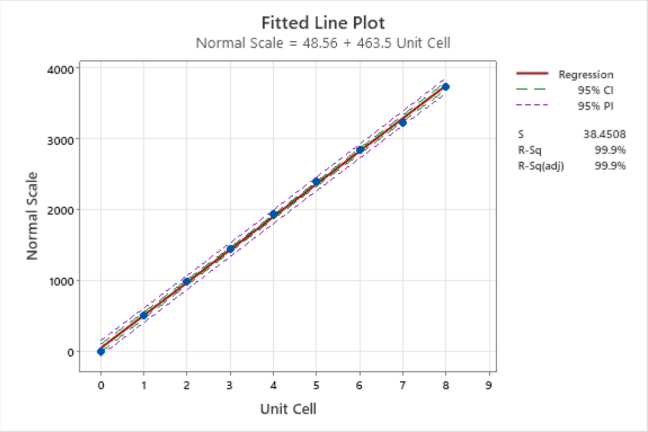

**Fig.23.** Normal scale unit cells lattice regression equation

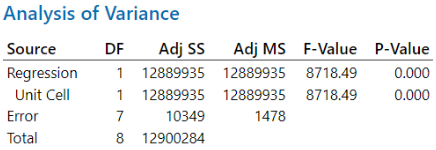

Analysis of Variance

| Source | DF | Adj SS | Adj MS | F-Value | P-Value |
|---|---|---|---|---|---|
| Regression | 1 | 12889935 | 12889935 | 8718.49 | 0.000 |
| Unit Cell | 1 | 12889935 | 12889935 | 8718.49 | 0.000 |
| Error | 7 | 10349 | 1478 | | |
| Total | 8 | 12900284 | | | |

**Fig.24.** ANOVA results of the relationship between unit cells Lattice normal scale and maximum force reaction during yielding

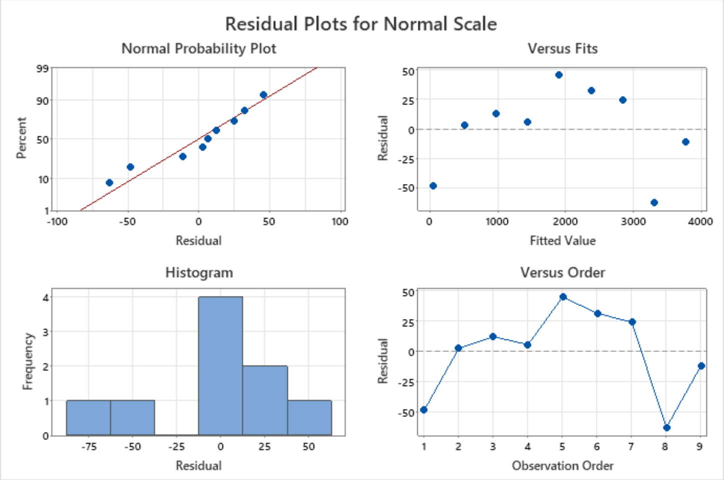

**Fig.25.** Validation of model assumptions (residual analysis) of the normal scale linear regression model

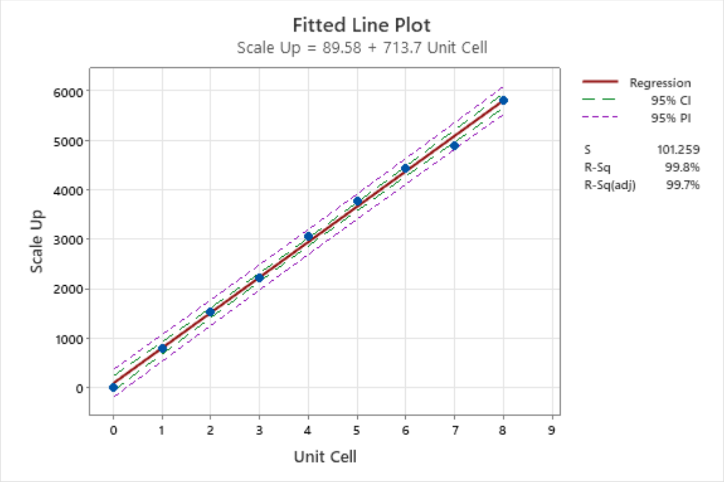

**Fig.26.** Scale up unit cells lattice regression equation

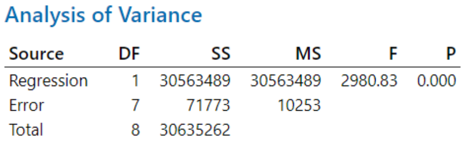

Analysis of Variance

| Source | DF | SS | MS | F | P |
|---|---|---|---|---|---|
| Regression | 1 | 30563489 | 30563489 | 2980.83 | 0.000 |
| Error | 7 | 71773 | 10253 | | |
| Total | 8 | 30635262 | | | |

**Fig.27.** ANOVA results of the relationship between unit cells lattice scale up and maximum force reaction during yielding

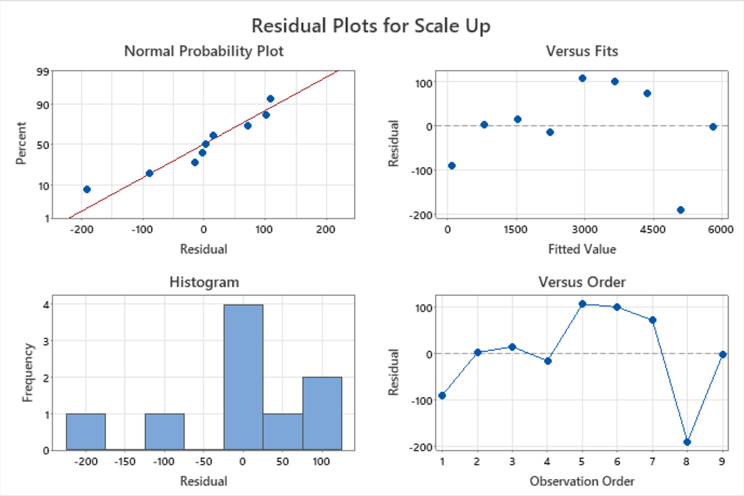

**Fig.28.** Validation of model assumptions (residual analysis) of the scale up regression model

Table 10. Results of linear regression analysis for each geometric scale

| Geometric Scale | Empirical Regression Equation | Coefficient of Determination ($R^2$) | P-Value | Force Factor per Cell (N/Cell) |
|---|---|---|---|---|
| *Scale-down* (3:4) | $F_{max} = 261.4 \times n_{cell} + 9.0$ | 99.77% | 0.000 | 261.4 |
| *Normal* (1:1) | $F_{max} = 463.5 \times n_{cell} + 48.6$ | 99.92% | 0.000 | 463.5 |
| *Scale-up* (5:4) | $F_{max} = 713.7 \times n_{cell} + 89.6$ | 99.77% | 0.000 | 713.7 |

All regression models demonstrated outstanding goodness-of-fit ($R^2 > 99.7\%$) and significant statistical relevance (model P-value = 0.000). The slope coefficient (m) for $n_{cells}$ was also very relevant in all models (P-value = 0.000). This means that the number of Unit Cells is a good linear predictor of the yield's reaction force.

When we look at the slope for $n_{cells} > 1$, the c values for all three models are not particularly big. The intercept is the theoretical yield force if there are no cells in a structure. It should be close to zero. The intercept values for the 0.75x and 1x scales are not statistically different from zero (P-value > 0.05), and they are only marginally significant for the 1.25x scale. This makes us more confident that the linear model shows that increasing the number of unit cells is what produces the significant load capacity.

### 3.4.4 Slope interpretation (empirical scale factor)

This study aims to determine the slope coefficient (m) for each regression equation: 261.40 N/cell at 0.75x, 463.50 N/cell at 1x, and 713.7 N/cell at 1.25x. The m value is the empirical scale factor, which is the average extra force that each new lattice cell at that geometric scale adds to the system's overall yield force. This result shows that the total load capacity increases as we add more of the same.

### 3.4.5 Interpretation of linear relationships and new design paradigms

The very high $R^2$ value is a key finding of this study. This finding allows the formulation of a new design paradigm that is more practical than the conventional stress concept. The slope coefficient of each regression equation (e.g., 463.5 N/cell for Normal Scale) can be physically interpreted as a "force factor per cell." This new metric allows an engineer to directly calculate the number of cells required to achieve the target load capacity, without requiring complex FEA analysis for each design iteration. For example, to support a load of 2000 N using a structure with a normal scale, the number of cells required with the same design geometry is approximately 2000 / 463.5 ≈ 4.3, so a design with five cells would be sufficient.

### 3.4.6 Quantitative analysis of effect size

With a scaling law model for each size, the effects of geometric scaling can be analyzed quantitatively. The increase in strength as the structure is scaled up should theoretically be proportional to the increase in the cross-sectional area of the strut, which is proportional to the square of its diameter ($A \propto d^2$). This theoretical ratio can be compared with the empirical ratio of the "force factor per cell" obtained from regression. This comparison is presented in Table 11.

Table 11. Quantitative analysis of effect size

| Scale Comparison | Theoretical Ratio (based on Strut Area) | Empirical Ratio (based on Force Factor/Cell) | Deviation |
|---|---|---|---|
| *Normal / Scale Down* | $2.0^2 / 1.5^2 = 1.778$ | 463.5 / 261.4 = 1.773 | -0.28% |
| *Scale Up / Normal* | $2.5^2 / 2.0^2 = 1.563$ | 713.7 / 463.5 = 1.540 | -1.47% |

The comparison shows that the empirical slope ratios obtained from the FEA simulations (1.773 and 1.540) are very close to the theoretical predictions based on quadratic scaling (1.778 and 1.563). This excellent agreement implies that, in the limit of FEA simulations with ideal geometry and linear-elastic material isotropic to yield, the scaling behaviour of this Octet-Truss lattice structure is dominated by macroscopic geometric changes (i.e., changes in effective cross-sectional area that scale with $n^2$), and intrinsic material size effects or micro-defect effects have not played a dominant role at the yield point. These results support the validity of the Similitude Theory approach in predicting force scaling under these ideal conditions, in line with the findings of Kasivitamnuay & Singhatanadgid (2017) [30] which shows that the scaling law applies even to non-linear materials if the similarity conditions are met.

## 4 Conclusion

This study conducted numerical analysis and experimental validation of the scaling rule for a PLA Octet-Truss lattice structure produced via FDM. The main conclusions are as follows:

1. Numerical simulations (FEA) provide remarkably accurate predictions of maximum compression force at yield with a mean absolute percentage error of 1.70% relative to experimental measurements. This minimal error demonstrates that the linear-elastic material model captures the elastic-to-plastic transition behaviour of the structures.
2. The primary failure mode observed is a combination of plastic buckling of individual struts and fracture, primarily at or near node connections. The location of this failure initiation qualitatively corresponds to the areas of high stress concentration predicted by the FEA model.
3. Linear regression analysis of the FEA data shows a robust positive linear relationship (R2  99.7%) and statistically significant (P-value = 0.000) relationship between the reaction force at the yield limit (Fsim) and the number of unit cells (ncell) for each geometric scale (0.75x, 1x, 1.25x).
4. The slope of this relationship increased with geometric scale, in excellent agreement with quadratic scaling predictions from the Theory of Similitude (1.778 and 1.563) for ideal simulation conditions.
5. The linear relationship Fsim ≈ m·ncell derived from FEA can be used as an effective initial prediction tool to estimate the load capacity of PLA Octet-Truss structures with different numbers of cells at a given geometric scale. However, due to the observed deviations during experimental validation, the application of safety factors based on validation error margin is highly recommended in practical engineering design to account for the influence of FDM defects and potential size effects on real structures.
6. This study is limited to the elastic–plastic transition regime and a fixed strut-to-cell diameter ratio using ESUN PLA+. Post-yield behavior, alternative materials, and other lattice topologies were not considered

## References

[1] A. Ramos, V. G. Angel, M. Siqueiros, T. Sahagun, L. Gonzalez, and R. Ballesteros, "Reviewing Additive Manufacturing Techniques: Material Trends and Weight Optimization Possibilities Through Innovative Printing Patterns," *Materials*, vol. 18, no. 6, p. 1377, Mar. 2025, doi: 10.3390/ma18061377.

[2] L. Ben Said, B. Ayadi, S. Alharbi, and F. Dammak, "Recent Advances in Additive Manufacturing: A Review of Current Developments and Future Directions," *Machines*, vol. 13, no. 9, p. 813, Sep. 2025, doi: 10.3390/machines13090813.

[3] Y. L. Chan *et al.*, "Review on 3D Printing Filaments Used in Fused Deposition Modeling Method for Dermatological Preparations," *Molecules*, vol. 30, no. 11, p. 2411, May 2025, doi: 10.3390/molecules30112411.

[4] I. Plamadiala, C. Croitoru, M. A. Pop, and I. C. Roata, "Enhancing Polylactic Acid (PLA) Performance: A Review of Additives in Fused Deposition Modelling (FDM) Filaments," *Polymers (Basel)*, vol. 17, no. 2, p. 191, Jan. 2025, doi: 10.3390/polym17020191.

[5] W. W. S. Ma *et al.*, "Multi-Physical Lattice Metamaterials Enabled by Additive Manufacturing: Design Principles, Interaction Mechanisms, and Multifunctional Applications," *Advanced Science*, vol. 12, no. 8, Feb. 2025, doi: 10.1002/advs.202405835.

[6] A. Kholil, G. Kiswanto, A. Al Farisi, and J. Istiyanto, "Finite Element Analysis of Lattice Structure Model with Control Volume Manufactured Using Additive Manufacturing," *International Journal of Technology*, vol. 14, no. 7, p. 1428, Dec. 2023, doi: 10.14716/ijtech.v14i7.6660.

[7] R. S. Khurmi and J. K. Gupta, *A Textbook of Machine Design*, vol. 14. New Delhi: Eurasia Publishing House (PVT) Ltd., 2005.

[8] T. Tancogne-Dejean and D. Mohr, "Elastically-isotropic truss lattice materials of reduced plastic anisotropy," *Int J Solids Struct*, vol. 138, pp. 24–39, May 2018, doi: 10.1016/j.ijsolstr.2017.12.025.

[9] V. S. Deshpande, N. A. Fleck, and M. F. Ashby, "Effective properties of the octet-truss lattice material," *J Mech Phys Solids*, vol. 49, no. 8, pp. 1747–1769, Aug. 2001, doi: 10.1016/S0022-5096(01)00010-2.

[10] F. Di Caprio, S. Franchitti, R. Borrelli, C. Bellini, V. Di Cocco, and L. Sorrentino, "Ti-6Al-4V Octet-Truss Lattice Structures under Bending Load Conditions: Numerical and Experimental Results," *Metals (Basel)*, vol. 12, no. 3, p. 410, Feb. 2022, doi: 10.3390/met12030410.

[11] Y. Li, H. Gu, M. Pavier, and H. Coules, "Compressive behaviours of octet-truss lattices," *Proc Inst Mech Eng C J Mech Eng Sci*, vol. 234, no. 16, pp. 3257–3269, Aug. 2020, doi: 10.1177/0954406220913586.

[12] G. Parodo, L. Sorrentino, S. Turchetta, and G. Moffa, "Evaluation of the Accuracy of a Fused Deposition Modeling Process in the Production of Low-Density ABS Lattice Structures," *Materials*, vol. 18, no. 7, p. 1679, Apr. 2025, doi: 10.3390/ma18071679.

[13] A. Alam, K. Berube, M. Rais-Rohani, and B. Khoda, "Mechanical Performance of Three-Dimensional Printed Lattice Structures: Assembled Versus Direct Print," *3D Print Addit Manuf*, vol. 10, no. 2, pp. 256–268, Apr. 2023, doi: 10.1089/3dp.2021.0207.

[14] A. R. Aziz, J. Zhou, D. Thorne, and W. J. Cantwell, "Geometrical Scaling Effects in the Mechanical Properties of 3D-Printed Body-Centered Cubic (BCC) Lattice Structures," *Polymers (Basel)*, vol. 13, no. 22, p. 3967, Nov. 2021, doi: 10.3390/polym13223967.

[15] M. C. Bedoya, J. W. Restrepo, L. V. Wilches, and J. Rodriguez, "Cellular Structures Analysis Under Compression Test," *Polymers (Basel)*, vol. 17, no. 11, p. 1476, May 2025, doi: 10.3390/polym17111476.

[16] L. Wang, Q. Chen, P. K. D. V. Yarlagadda, F. Zhu, Q. Li, and Z. Li, "Single-parameter mechanical design of a 3D-printed octet truss topological scaffold to match natural cancellous bones," *Mater Des*, vol. 209, p. 109986, Nov. 2021, doi: 10.1016/j.matdes.2021.109986.

[17] W. Liu, H. Song, Z. Wang, J. Wang, and C. Huang, "Improving mechanical performance of fused deposition modeling lattice structures by a snap-fitting method," *Mater Des*, vol. 181, p. 108065, Nov. 2019, doi: 10.1016/j.matdes.2019.108065.

[18] A. Casaburo, G. Petrone, F. Franco, and S. De Rosa, "A Review of Similitude Methods for Structural Engineering," *Appl Mech Rev*, vol. 71, no. 3, May 2019, doi: 10.1115/1.4043787.

[19] M. Melchiorre and T. Duncan, "The Fundamentals of FEA Meshing for Structural Analysis," Ansys. Accessed: Nov. 01,

2025. [Online]. Available: https://www.ansys.com/blog/fundamentals-of-fea-meshing-for-structural-analysis

[20] Ansys, "Lecture 7: Mesh Quality & Advanced Topics ," in *Introduction to ANSYS Meshing*, 2015. Accessed: Oct. 27, 2025. [Online]. Available: https://featips.com/wp-content/uploads/2021/05/Mesh-Intro_16.0_L07_Mesh_Quality_and_Advanced_Topics.pdf

[21] ESUN, "ESUN PLA+ Technical Data Sheet," Guangdong, Nov. 2021. Accessed: Oct. 06, 2025. [Online]. Available: https://www.esun3d.com/uploads/eSUN_PLA+-Filament_TDS_V4.0.pdf

[22] P. Newman, "Static Structural Analysis," Ansys. Accessed: Oct. 06, 2025. [Online]. Available: Static Structural Analysis

[23] A. Cunha, Y. Yanik, C. Olivieri, and S. da Silva, "Tresca Versus Von Mises: Which Failure Criterion is More Conservative in a Probabilistic Context?," *J Appl Mech*, vol. 91, no. 11, Nov. 2024, doi: 10.1115/1.4063894.

[24] H. P. Gavin, "Strain Energy in Linear Elastic Solids," in *Matrix Structural Analysis*, Duke University Department of Civil and Environmental Engineering, 2012.

[25] T. H. G. Megson, "Stress and Strain," in *Structural and Stress Analysis*, Elsevier, 2014, pp. 146–183. doi: 10.1016/B978-0-08-099936-4.00007-3.

[26] J. Mueller and K. Shea, "Buckling, build orientation, and scaling effects in 3D printed lattices," *Mater Today Commun*, vol. 17, pp. 69–75, Dec. 2018, doi: 10.1016/j.mtcomm.2018.08.013.

[27] ASTM International, "ASTM D695-23 - Test Method for Compressive Properties of Rigid Plastics," Aug. 01, 2023, *West Conshohocken, PA*. doi: 10.1520/D0695-23.

[28] A. Jierula, S. Wang, T.-M. OH, and P. Wang, "Study on Accuracy Metrics for Evaluating the Predictions of Damage Locations in Deep Piles Using Artificial Neural Networks with Acoustic Emission Data," *Applied Sciences*, vol. 11, no. 5, p. 2314, Mar. 2021, doi: 10.3390/app11052314.

[29] Douglas C. Montgomery, *Design and Analysis of Experiment Ninth Edition*. Arizona State University: John Wiley & Sons, Inc., 2017.

[30] J. Kasivitamnuay and P. Singhatanadgid, "Scaling laws for displacement of elastic beam by energy method," *Int J Mech Sci*, vol. 128–129, pp. 361–367, Aug. 2017, doi: 10.1016/j.ijmecsci.2017.05.001.